

# Optoelectronic neuro-synaptic behaviors of antiferroelectric $\text{NaNbO}_3/\text{n-GaN}$ heterostructures

Huijuan Dong (董慧娟)<sup>1,2</sup>, Kexin Jin (金克新)<sup>2</sup>, and Bingcheng Luo (罗炳成)<sup>2\*</sup>

<sup>1</sup>Department of Physics, Changzhi University, Changzhi 046011, China

<sup>2</sup>School of Physical Science and Technology, Northwestern Polytechnical University, Xi'an 710072, China

\*Corresponding author: [luobingcheng@nwpu.edu.cn](mailto:luobingcheng@nwpu.edu.cn)

Received February 4, 2025 | Accepted May 8, 2025 | Posted Online May 30, 2025

The development of artificial synaptic devices that emulate synaptic activity is key to advancing the hardware implementation of neuromorphic computing. In this study, we present an optoelectronic synaptic device based on a  $\text{NaNbO}_3/\text{n-GaN}$  heterostructure, which exhibits defect-dominated carrier transport behaviors. This device effectively demonstrates typical synaptic functions, including paired-pulse facilitation, short-term memory, long-term memory, human cognitive behavior, and human visual memory, using both optical and electrical stimuli. These results highlight the potential of the  $\text{NaNbO}_3/\text{n-GaN}$  heterostructure for future neuromorphic systems.

**Keywords:** sodium niobate; optoelectronic synapse; synaptic plasticity; heterostructure.

**DOI:** [10.3788/COL202523.062502](https://doi.org/10.3788/COL202523.062502)

## 1. Introduction

Digital computers based on the von Neumann architecture have achieved remarkable progress, excelling at solving structured problems. However, with the exponential growth of data, traditional computer systems face significant challenges stemming from the so-called “von Neumann bottleneck”<sup>[1–3]</sup>. Neuromorphic computing, inspired by the human brain’s functionality, has emerged as a promising solution, particularly for applications in Internet of Things (IoT) and artificial intelligence (AI)<sup>[4–7]</sup>. Realizing neuromorphic computing at the hardware level requires the development of integrated memory-computing devices that mimic the structure and function of biological synapses, enabling efficient and high-speed computing capacity akin to the human brain.

Artificial synapses aim to mimic the dynamic learning and memory processes of biological synapses by programmed stimuli, enabling brain-like neuromorphic computation. Optoelectronic synaptic devices leverage optical stimuli or a combination of optical and electrical stimuli to emulate synaptic functions<sup>[8–10]</sup>. Compared to electrical stimuli, optical stimuli offer distinct advantages, such as ultra-high speed, wide bandwidth, and minimal crosstalk<sup>[11–13]</sup>. These characteristics make optoelectronic neuromorphic devices a promising avenue for achieving ultra-low-power and ultra-high-speed neuromorphic computation, positioning them as a growing focus in this field<sup>[14,15]</sup>.

To date, researchers have developed a wide range of optoelectronic synaptic devices using diverse materials, device

architectures, and modulation modes. For example, Agnus *et al.*<sup>[16]</sup> in 2010 introduced a carbon-nanotube-based photo-transistor that mimicked biological synaptic function, laying the foundation for artificial photoelectric synapse research. Since then, various device structures, including memristors, thin film transistors, phase-change memories, and ferroelectric memories, have been explored to simulate optoelectronic synapses<sup>[17–23]</sup>. The operating mechanism of most optoelectronic neurosynaptic devices is rooted in defects and carrier traps or potential wells within materials<sup>[24,25]</sup>. The trapping and detrapping of carriers by defect states drive persistent photoconductivity (PPC) effects, enabling the emulation of synaptic functions. Consequently, the deliberate introduction of defect states through material selection and structural design has become a key strategy in advancing optoelectronic neurosynaptic devices.

Sodium niobate ( $\text{NaNbO}_3$ , NNO), a lead-free niobium-based antiferroelectric, has attracted significant attention for its complex phase transition behavior and potential in energy storage applications<sup>[26–28]</sup>. However, the volatile nature of sodium in NNO often leads to defect formation during heat treatment, which can degrade its energy storage performance. Interestingly, these defects, which facilitate the trapping and release of carriers, are also highly relevant for simulating synaptic functions. For example, studies on other lead-free niobium-based ferroelectrics, such as  $(\text{Na}_{1-x}\text{K}_x)\text{NbO}_3$  and  $\text{KNbO}_3$  memristors, have demonstrated their resistive switching (ReRAM) and synaptic properties, validating their potential as artificial synapses<sup>[29–31]</sup>. As for NNO, Gaggio *et al.*<sup>[32]</sup> investigated a double-layer  $\text{NaNbO}_3/\text{Nb}_2\text{O}_5$ , demonstrating the  $\text{Na}^+$  control of interfacial

resistive switching (RS). Both spike-amplitude and spike-time-dependent measurements dynamically controlled by  $\text{Na}^+$  showed biological synaptic plasticity. Kim *et al.*<sup>[33]</sup> deposited [001]-oriented  $\text{NaNbO}_3$  thin films on  $\text{Sr}_2\text{Nb}_3\text{O}_{10}/\text{TiN}/\text{SiO}_2/\text{Si}$  substrates by the Langmuir-Blodgett technique and observed the bipolar switching behavior. In addition, the memristor can mimic synaptic properties of biological synapses, suggesting that it can be used in neuromorphic computing systems. Despite this progress, the potential of NNO for artificial synaptic applications remains largely unexplored.

In this work, we present an optoelectronic synaptic device based on NNO/n-GaN heterostructure, which is capable of emulating various biological synaptic functions, including long-term potentiation (LTP), long-term depression (LTD), paired-pulse facilitation (PPF), short-term memory (STM) to long-term memory (LTM) conversion, human cognitive behavior, and visual memory.

## 2. Experiment

NNO thin films were fabricated on free-standing n-type GaN substrates via a sol-gel method. The preparation of the precursor solution with a concentration of 0.3 mol/L has been detailed in prior work<sup>[34]</sup>. For deposition, the precursor solution was deposited on  $5\text{ mm} \times 5\text{ mm}$  n-type GaN substrates and spin-coated at 5500 rpm (r/min) for 30 s. A total of three layers were deposited, with each layer dried on a hot plate at  $120^\circ\text{C}$  for 5 min. Following deposition, the films were annealed at  $500^\circ\text{C}$  for 5 min under an oxygen atmosphere in a rapid annealing furnace, using a heating rate of  $10^\circ\text{C}/\text{s}$ . Top Pt circular electrodes with a diameter of 0.2 mm and a thickness of 10 nm were sputtered onto the NNO film surface to form the Pt/NNO/n-GaN device.

The film thickness, crystalline structure, and surface topography were analyzed using a cross-scanning electron microscope (SEM, FEI Verios G4), a grazing incidence X-ray diffraction (GIXRD, PANalytical Empyrean), and an atomic force microscope (AFM, Asylum Research MFP-3D), respectively. The ferroelectric, dielectric, and current-voltage (I-V) properties were studied using a ferroelectric tester (Radiant Technologies Precision LC II), an LCR meter (Agilent E4980), and a picoammeter voltage source (Keithley 6487). The 330 nm laser was used as an excitation source for optoelectronic measurements.

## 3. Results and Discussion

### 3.1. Characterization of $\text{NaNbO}_3/\text{n-GaN}$ heterostructure

Figure 1(a) depicts the GIXRD pattern of the NNO thin film deposited directly on the n-type GaN substrate. Aside from the peak at  $38.22^\circ$  attributed to the GaN substrate, all other diffraction peaks correspond to a polycrystalline orthorhombic perovskite structure, consistent with the standard  $\text{NaNbO}_3$  spectrum at the bottom (JCPDS No: 74-2454). No secondary phases or apparent preferred orientation were detected. The cross-SEM image shown in Fig. 1(b) reveals that the NNO thin film has a thickness of approximately 200 nm. The surface of the NNO thin film is dense and smooth, as shown in Fig. S1 in the [Supplementary Material](#).

Figure 1(c) shows the polarization-electric (P-E) field hysteresis loop of the Pt/NNO/n-GaN device, demonstrating a ferroelectric-like behavior. This characteristic is commonly attributed to the field-induced metastable ferroelectric phase, which persists even after the external electric field is removed<sup>[35]</sup>. Under an electric field of  $\pm 300\text{ kV}/\text{cm}$ , the remnant polarization and coercive field were obtained to  $3.8\text{ }\mu\text{C}/\text{cm}^2$  and  $30\text{ kV}/\text{cm}$ ,

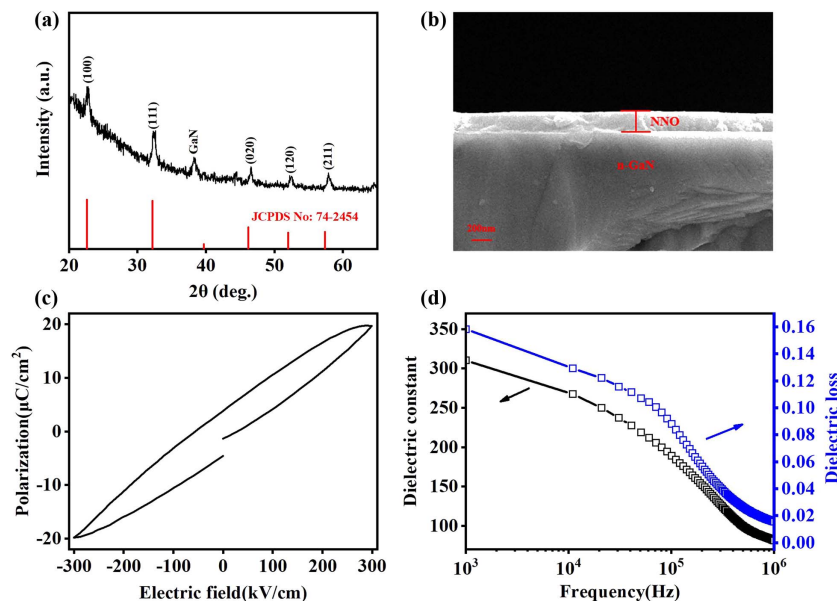


**Fig. 1.** Characterization of NNO/n-GaN heterostructure. (a) XRD pattern. (b) Cross-SEM image. (c) The polarization-electric [P-E] field hysteresis loop at 1 kHz. (d) Frequency-dependent dielectric constant and loss.

respectively. The polarization value is comparable to the values obtained in the literature<sup>[36,37]</sup>. The frequency-dependent dielectric constant and loss are shown in Fig. 1(d). The relative dielectric constant ( $\epsilon_r$ ) and dielectric loss ( $\tan \delta$ ) were determined to be 310 and 0.16 at 1 kHz. As the frequency increases from 1 kHz to 1 MHz, both the dielectric constant and loss decrease, indicating typical dielectric relaxation behavior. The dielectric relaxation behavior is attributed to the space charge polarization effect<sup>[38,39]</sup>. NaNbO<sub>3</sub> has a perovskite structure, while GaN has a hexagonal wurtzite structure. The lattice mismatch and possible interdiffusion between the NNO thin film and the GaN substrate result in a significant number of interfacial defects<sup>[40,41]</sup>. These defects often act as carrier traps, impeding carrier mobility and accommodating space charges. At higher frequencies, the space charge polarization cannot follow the external electric field, leading to dielectric dispersion.

A memristor that exhibits resistive switching behavior is essential for emulating artificial synapses<sup>[42]</sup>. To investigate this, the I-V characteristics of the Pt/NNO/n-GaN device were measured under a voltage sweep from 0 V → 3.0 V → 0 V → -3.0 V → 0 V. As shown in Fig. 2(a), the device initially remains in a high-resistance state (HRS) at positive voltage. When the applied voltage increases, the device transitions from HRS to a low-resistance state (LRS), demonstrating typical resistive switching (RS) behavior. This behavior is closely related to the defect states in Pt/NNO/n-GaN devices. Additionally, the I-V curves exhibit significant asymmetry under positive and negative biases. The asymmetry is likely due to the distinct work functions flanking the NNO layer. Specifically, the electron affinities of NNO and n-type GaN are 3.53<sup>[43]</sup> and 4.2 eV<sup>[44]</sup>, respectively. Pt has a work function of ~5.65 eV<sup>[45]</sup>. The corresponding band energy

alignment is illustrated in Fig. S2 in the [Supplementary Material](#). Further, the leakage mechanism was analyzed using common conduction models for dielectric oxide films<sup>[46]</sup>. The double logarithmic I-V curves of the device in Fig. 2(b) reveal three distinct linear regions with varying slopes. At low voltages, the device exhibits ohmic conduction behavior ( $I \propto V$ ), indicating that thermally generated free carriers dominate. As the voltage increases, the curve follows Child's law ( $I \propto V^2$ ), suggesting that charge carriers injected from the electrodes fill the trap states. At even higher voltages, the slope of the fitted line increases sharply to values greater than two, marking the trap filling limit voltage ( $V_{TFL}$ ). This voltage is determined by<sup>[47]</sup>

$$V_{TFL} = \frac{qN_t d^2}{2\epsilon_r \epsilon_0}, \quad (1)$$

where  $N_t$  is the trap state density,  $\epsilon_r$  is the dielectric constant of NaNbO<sub>3</sub>,  $\epsilon_0$  is the vacuum dielectric constant,  $d$  is the film thickness, and  $q$  is the element charge. Under positive and negative biases, the  $V_{TFL}$  values are around 2.3 and 1.8 V, respectively. This disparity is primarily attributed to the interfacial defects between the NNO thin films and the n-type GaN substrate. Using a dielectric constant of 670 for NaNbO<sub>3</sub><sup>[48]</sup>, the calculated trap state density ( $N_t$ ) of the Pt/NNO/n-GaN device is  $3.3 \times 10^{18}$ – $4.2 \times 10^{18}$  cm<sup>-3</sup>. Additionally, the trap states in the thin film are associated with oxygen vacancies, as suggested by the X-ray photoelectron spectroscopy (XPS), shown in Fig. S3 in the [Supplementary Material](#).

Additionally, we investigated the transient current characteristics of the Pt/NNO/n-GaN device under 330 nm light irradiation with an intensity of 2.7 μW/mm<sup>2</sup>. As shown in Fig. 2(c),

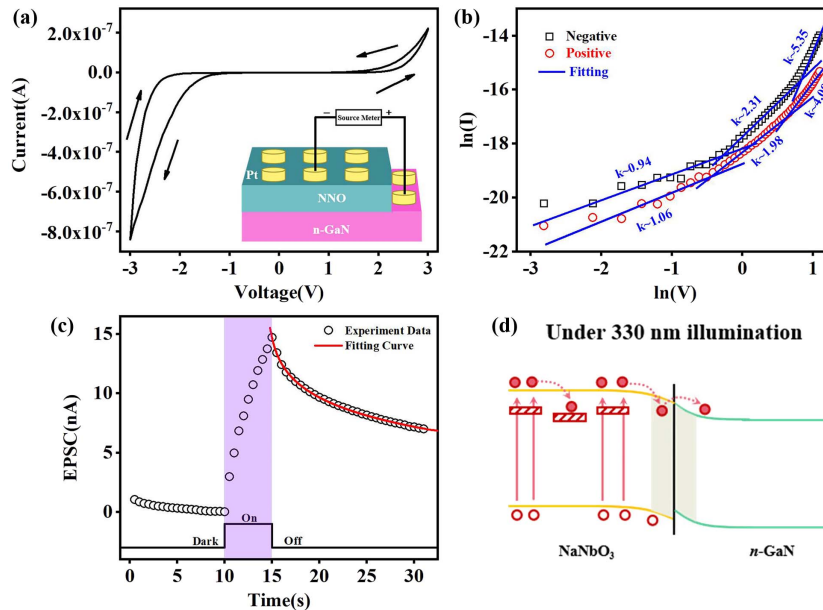


**Fig. 2.** Photoelectric performance of NNO/n-GaN heterostructure. (a) Current-voltage (I-V) hysteresis loop (the inset shows the schematic diagram of the I-V measurement). (b) Ln(I)-Ln(V) curves. (c) Typical device optical switching characteristics under the 330 nm light with an intensity of 2.7 μW/mm<sup>2</sup>. (d) Energy-band diagrams of optical responses.

5 s of continuous light exposure results in a considerable current increase ( $\Delta I$ ) of 15 nA; the increase in current caused by the optical signal represents the generation of excitatory postsynaptic current (EPSC). After the light source is turned off, the current gradually decreases, reaching 62.8% of its peak value after 15 s in darkness. The decay rate then slows, and the current cannot return to its initial value, indicative of a persistent photoconductive (PPC) effect. This current decay can be fitted using the Kohlrausch exponential function<sup>[49]</sup>:

$$I_t = \Delta I \times \exp[-(t/\tau)^\beta] + I_c, \quad (2)$$

where  $\tau$  is the relaxation time and  $\beta$  is the stretching index (ranging between zero and one). The background current,  $I_c$ , was set to zero. The fitted relaxation time  $\tau$  of approximately 1177 s and a retention time exceeding 3000 s (Fig. S4 in the [Supplementary Material](#)) demonstrate the non-volatility of the device, highlighting its potential for photonic synapses and neuromorphic computing. The stretching index  $\beta$  was determined to be  $0.17 \pm 0.01$ . The response mechanism under light illumination is illustrated in Fig. 2(d). Due to the work function mismatch between n-GaN and NNO, a band bending occurs at their interface. Under light stimulation, photons excite electrons from the valence band to the conductive band, forming electron-hole pairs. Their pairs are separated by the applied electric field. Specifically, holes migrate to the Pt electrode, while electrons migrate to the n-GaN but are captured by defects in the NNO and at the interface. After light stimulation ceases, trapped electrons are gradually released, transitioning to the conductive band as free electrons. These electrons then recombine with holes in the valence band. However, the thermal release of

trapped electrons requires a relaxation time, which prevents the device's conductivity from fully returning to its initial state, therefore manifesting the PPC effect.

### 3.2. Electronic synaptic plasticity

Figure 3(a) illustrates the I-V characteristics of the Pt/NNO/n-GaN device over 10 cycles of negative voltage sweeps ( $0 \text{ V} \rightarrow -3 \text{ V} \rightarrow 0 \text{ V}$ ), with n-type GaN serving as the bottom electrode and Pt as the top electrode. As the number of voltage sweeps increases, the current gradually decreases and approaches saturation. Such continuous, tunable conductance changes are a hallmark of memristor operation, suggesting the device's potential to mimic biological synapses. To explore this potential, the device was subjected to 30 identical positive pulses (10 V, 0.05 ms) followed by 30 negative pulses ( $-3 \text{ V}$ , 0.05 ms), each separated by a 0.05 ms interval, as shown in Fig. 3(b). The current progressively increases during the application of positive voltage pulses and decreases with negative voltage pulses, replicating the LTP and LTD behaviors observed in biological synapses. This implies that the Pt/NNO/n-GaN device exhibits robust synaptic plasticity, making it a promising candidate for neuromorphic computing applications.

Short-term plasticity (STP) and LTP are the two main forms of synaptic plasticity, essential for the memory functions in biological nervous systems<sup>[50]</sup>. The PPF is commonly used to characterize the STP<sup>[51]</sup>. When two successive pulses are applied to a presynaptic neuron, the response amplitude of the second pulse is significantly larger than that of the first pulse. This phenomenon is critical for processing synaptic information in biological systems. The amplitude of the second pulse depends on the time interval ( $\Delta t$ ) between the two pulses, where shorter intervals

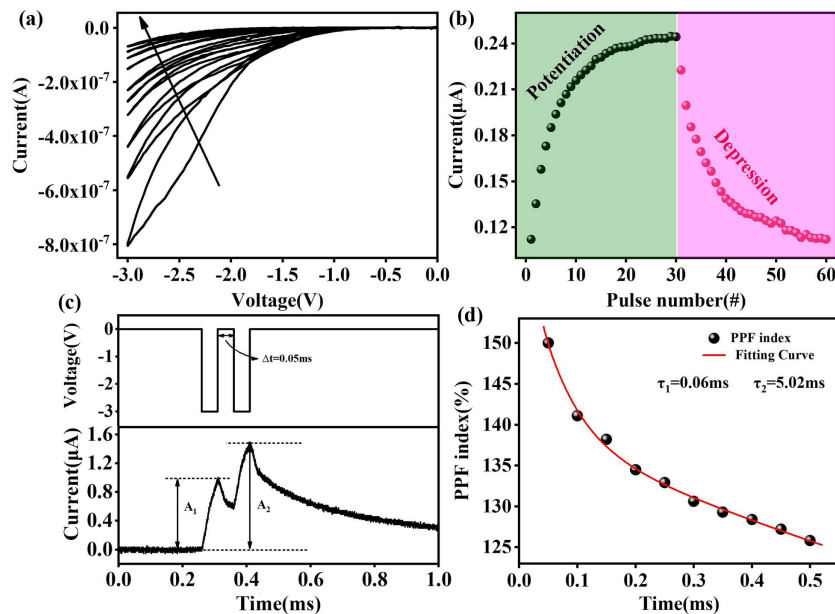


**Fig. 3.** Electronic synaptic plasticity performances of NNO/n-GaN heterostructure. (a) I-V hysteresis under consecutive dual negative voltage sweeps. (b) Synaptic potentiation and synaptic depression triggered by electric stimuli. (c) PPF phenomenon. (d) Electrical PPF index versus time interval between successive pulses and fitting curves.

produce stronger facilitation effects. The PPF index quantifies the change in conductance and is defined as<sup>[52]</sup>

$$PPF = (A_2/A_1) \times 100\%, \quad (3)$$

where  $A_1$  is the peak amplitude of the first pulse and  $A_2$  is the peak amplitude of the second pulse. As shown in Fig. 3(c), the PPF index is around 149.9% when the device responds to two successively applied negative pulses ( $-3$  V, 0.05 ms) with a time interval of  $\Delta t = 0.05$  ms. Additionally, the relationship between the PPF index and the time interval  $\Delta t$  is shown in Fig. 3(d). The PPF index decreases with increasing  $\Delta t$ , which can be described using a double-exponential decay function:

$$PPF = C_1 e^{-t/\tau_1} + C_2 e^{-t/\tau_2} + 1, \quad (4)$$

where  $C_1$  and  $C_2$  are the initial facilitation magnitudes, and  $\tau_1$  and  $\tau_2$  represent characteristic times. From the fitting results,  $\tau_1$  and  $\tau_2$  are determined to be 0.06 and 5.02 ms, respectively. Notably,  $\tau_2$  is at least an order of magnitude larger than  $\tau_1$ , a trend consistent with biological synaptic behavior<sup>[53]</sup>.

### 3.3. Photonic synaptic plasticity

Figure 4(a) illustrates a schematic of the biological synapses connecting two neurons and a schematic diagram for testing the optical synaptic properties of the Pt/NNO/n-GaN device. A fixed direction light source with a 330 nm wavelength is irradiated on the film's surface. Similar to electrical stimulation, the Pt/NNO/n-GaN device also exhibits a light-induced PPF, as shown in Fig. 4(b). The PPF index is around 137% for two consecutive light pulses (light intensity:  $2.7 \mu\text{W}/\text{mm}^2$ ; light duration: 5 s; time interval  $\Delta t$ : 5 s). The amplitude of the current change is related to

the time interval  $\Delta t$  between the two pulses. This behavior highlights the potential of the Pt/NNO/n-GaN device as an artificial optoelectronic synapse, where the optical pulse inputs act as pre-synaptic spikes, device currents reflect synaptic weights, and optical response currents represent postsynaptic currents. In Fig. 4(c), the PPF index ( $A_2/A_1$ , represented by black solid circles) is plotted against the time interval ( $\Delta t$ ) between light pulses. The experimental data aligns well with the curve (red solid line) obtained using Eq. (4). The fitting yields characteristic times of  $\tau_1 = 4$  s and  $\tau_2 = 339$  s. Notably,  $\tau_2$  is more than an order of magnitude larger than  $\tau_1$ , consistent with the features observed in biological synapses<sup>[54]</sup>.

Organisms store information in the brain through rehearsed learning processes, with the strength of memory retention largely determined by the intensity and frequency of learning, as illustrated in Fig. 5(a). Memory activity is typically classified into two categories based on retention time: STM and LTM, both of which are related to synaptic plasticity<sup>[55]</sup>. STM, characterized by lower synaptic weights, is stored in the hippocampus for seconds to minutes. With repeated training and rehearsal, STM transitions to LTM where information is preserved in the cerebral cortex for hours to years. To replicate STM, LTM, and the STM-to-LTM transition, the Pt/NNO/n-GaN device is subjected to a series of light pulse stimuli (wavelength: 330 nm, light intensity:  $2.7 \mu\text{W}/\text{mm}^2$ , light retention time: 5 s) with varying pulse numbers ( $N$ ) and frequencies ( $f$ ). As shown in Fig. 5(b), the EPSC decreases from  $\sim 29$  to  $\sim 15$  nA over a 10 s period when applying a single pulse ( $N = 1$ ), confirming STM behavior. As the pulse number increases, EPSC increases. For  $N = 50$ , EPSC stabilizes at  $\sim 58$  nA after light stimulation, demonstrating LTM behavior. Similarly, the STM-to-LTM transition is observed when the device is stimulated with light pulses of varying frequencies

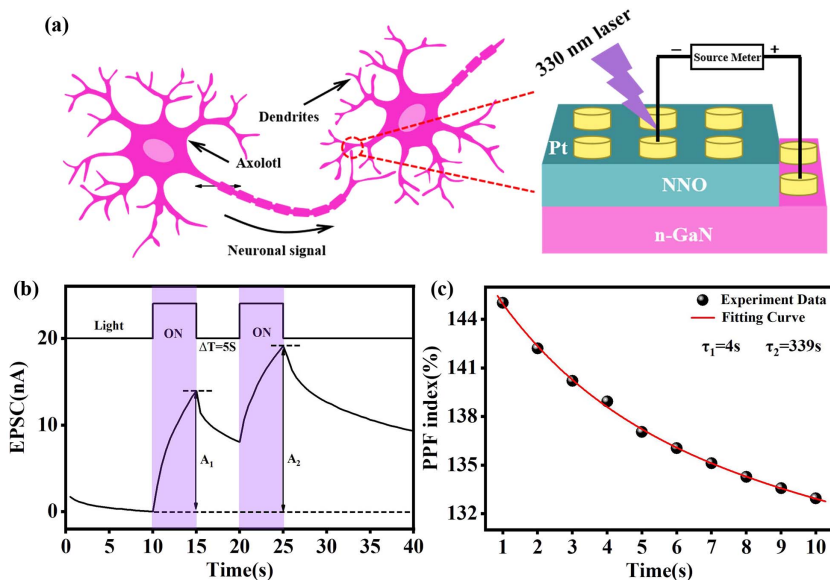
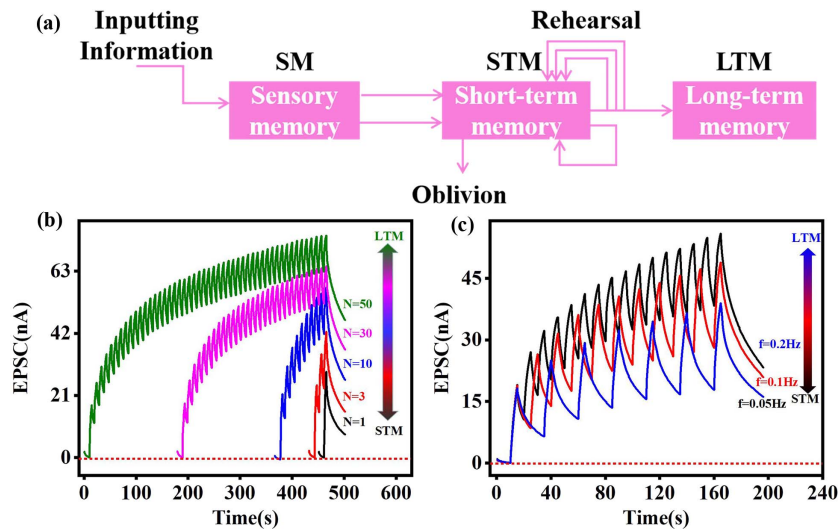


Fig. 4. Photo-induced PPF behavior in NNO/n-GaN heterostructure. (a) Neural signal transmission at biological synapses and device structure diagram. (b) Typical photoresponsive characteristic under a light pulse pair with a 5 s interval. (c) Photonic PPF index versus time interval ( $\Delta t$ ) between successive pulses.



**Fig. 5.** Mimicking STM and LTM using NNO/n-GaN heterostructure. (a) Schematic diagram showing the biological memory consolidation process in the human brain. STM-to-LTM transition induced by increasing (b) number and (c) frequency of pulsed light stimuli.

[Fig. 5(c)], as well as intensities and retention times (Fig. S5 in the [Supplementary Material](#)). Additionally, the decay behavior with different pulse numbers, light frequencies, light intensities, and light retention times is shown in Fig. S6 in the [Supplementary Material](#). The current decay process under multiple optical stimuli is fitted using the stretched exponential function [Eq. (2)]. A larger  $\tau$  indicates denser memory storage and slower forgetting rates. As shown in Fig. S7 in the [Supplementary Material](#), the characteristic time  $\tau$  and EPSC positively correlate with pulse number, light frequency, light intensity, and light retention time, confirming the STM-to-LTM transition. These results demonstrate that the Pt/NNO/n-GaN device is capable of performing advanced memory tasks under simulated light signals, making it suitable for artificial optoelectronic synapses.

The process of learning and forgetting in the human brain follows the principles outlined by the Ebbinghaus forgetting curve, demonstrating that memory retention is time-dependent<sup>[56]</sup>.

Repeated cycles of learning and forgetting enable the transformation of STM into LTM<sup>[57]</sup>. In this process, new knowledge is acquired through learning but gradually fades over time. However, relearning the same information takes less time to achieve the previous level of proficiency, illustrating the concept of “learning-experience”. As shown in Fig. 6, during the first learning cycle, the device is stimulated with 50 repeated light pulses, resulting in a significant increase in synaptic weights. Following stimulation, the synaptic weights spontaneously decay, mimicking the partial forgetting of information over time in humans. To recover the reduced synaptic weights, the device undergoes a second stimulation using the same pulse width and optical pulse frequency. Remarkably, only nine pulses are needed to restore the synaptic weights to their prior maximum value, compared to the 43 pulses needed during the initial learning process. Additionally, after the second stimulation, the synaptic weight loss over the 50 s period is significantly less than that observed following the first stimulation. This demonstrates

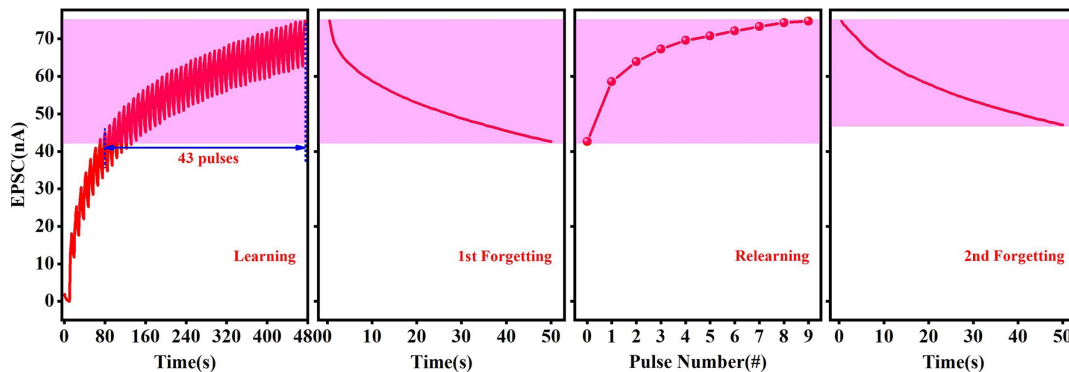


**Fig. 6.** “Learning-experience” behavior of NNO/n-GaN heterostructure. The current increase with the number of optical pulses corresponds to the learning or relearning process, while the current decay after the light stimulation represents the forgetting process. Optical pulse parameters: light wavelength: 330 nm; intensity:  $2.7 \mu\text{W}/\text{mm}^2$ ; pulse width: 5 s; frequency: 0.2 Hz.

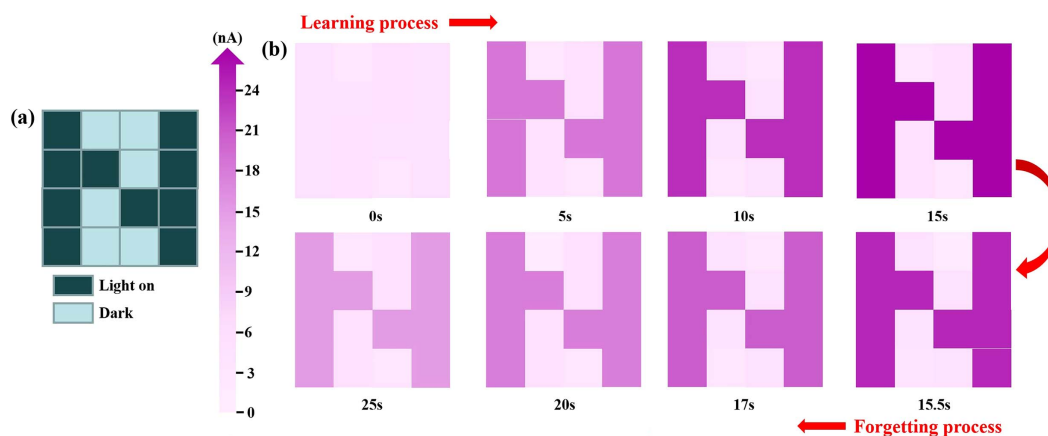


Fig. 7. Emulation of visual memory function in NNO/n-GaN heterostructure. (a) Image mapping of N-shaped  $4 \times 4$  array. (b) Dynamic learning and forgetting process of conductance response image mapping.

the device's ability to emulate the human brain's learning-experience behavior.

The Pt/NNO/n-GaN device demonstrates remarkable light sensitivity, making it a promising candidate for mimicking human vision. As shown in Fig. 7(a), a  $4 \times 4$  N-shaped photosynaptic array is utilized to demonstrate the dynamic learning and forgetting processes. The evolution of the conductance under light pulse stimulation is depicted in Fig. 7(b). With longer light retention time, the "N" pattern becomes progressively encoded in the synaptic array, representing a dynamic learning process where the retention time simulates varying durations of visual exposure. After a 15 s learning period, the forgetting process begins. Initially, forgetting occurs rapidly, but the decay rate gradually slows over time.

#### 4. Conclusion

In conclusion, NNO thin films were successfully integrated with n-type GaN semiconductor substrates using a sol-gel method to fabricate the Pt/NNO/n-GaN device. The thin films exhibit a compact uniform surface and an orthorhombic perovskite structure. The device demonstrates typical ferroelectric properties, and the dielectric constant and loss decrease with increasing frequency. Analysis of the leakage current mechanism reveals that the trap-related space charge-limiting current mechanism governs the Pt/NNO/n-GaN devices, with a calculated trap state density of about  $3.3 \times 10^{18}$ – $4.2 \times 10^{18} \text{ cm}^{-3}$ . The device also exhibits resistance switching behavior attributed to charge trapping and detrapping processes, enabling it to mimic biological synaptic functions. Leveraging its memory properties, the device successfully realizes artificial photoelectric synapses and visual memory functions. It replicates fundamental synaptic functions, such as PPF, LTP, LTD, STM, and LTM transitions under electrical and optical stimulation. Additionally, human visual memory is successfully simulated using a  $4 \times 4$  synaptic array, further showcasing its versatility. These results highlight the Pt/NNO/n-GaN device as a promising candidate for in-sensor computing.

#### Acknowledgements

This work was supported by the Shanxi Provincial Basic Research Program (No. 202303021212272). H. D. acknowledges support of the National Natural Science Foundation of China (No. 52333009).

#### References

1. Y. Liu, Y. Wu, H. Han, *et al.*, "CuInP<sub>2</sub>S<sub>6</sub>-based electronic/optoelectronic synapse for artificial visual system application," *Adv. Funct. Mater.* **34**, 2306945 (2023).
2. L. Dong, S. Yuan, G. Wei, *et al.*, "Artificial optoelectronic synapse based on violet phosphorus microfiber arrays," *Small* **20**, 2306998 (2024).
3. M. Islam, D. Dev, A. Krishnaprasad, *et al.*, "Optoelectronic synapse using monolayer MoS<sub>2</sub> field effect transistors," *Sci. Rep.* **10**, 21870 (2020).
4. L. Jiang, G. Lu, Y. Zeng, *et al.*, "Flexible ultrasound-induced retinal stimulating piezo-arrays for biomimetic visual prostheses," *Nat. Commun.* **13**, 3853 (2022).
5. X. Liu, D. Wang, W. Chen, *et al.*, "Optoelectronic synapses with chemical-electric behaviors in gallium nitride semiconductors for biorealistic neuromorphic functionality," *Nat. Commun.* **15**, 7671 (2024).
6. F. Liao, Z. Zhou, B. J. Kim, *et al.*, "Bioinspired in-sensor visual adaptation for accurate perception," *Nat. Electron.* **5**, 84 (2022).
7. X. Pan, Y. Li, B. Cheng, *et al.*, "2D materials for intelligent devices," *Sci. China-Phys. Mech. Astron.* **66**, 117504 (2023).
8. C. Choi, J. Leem, M. Kim, *et al.*, "Curved neuromorphic image sensor array using a MoS<sub>2</sub>-organic heterostructure inspired by the human visual recognition system," *Nat. Commun.* **11**, 5934 (2020).
9. J. Meng, T. Wang, H. Zhu, *et al.*, "Integrated in-sensor computing optoelectronic device for environment-adaptable artificial retina perception application," *Nano Lett.* **22**, 81 (2022).
10. C. Lu, J. Meng, J. Song, *et al.*, "Self-rectifying all-optical modulated optoelectronic multistates memristor crossbar array for neuromorphic computing," *Nano Lett.* **24**, 1667 (2024).
11. Z. D. Luo, X. Xia, M. M. Yang, *et al.*, "Artificial optoelectronic synapses based on ferroelectric field-effect enabled 2D transition metal dichalcogenide memristive transistors," *ACS Nano* **14**, 746 (2020).
12. X. Han, Y. Mo, B. Wang, *et al.*, "Amorphous Ga<sub>2</sub>O<sub>3</sub>/GaN heterostructure for ultalow-energy-consumption optically stimulated synaptic devices," *Appl. Phys. Lett.* **124**, 013502 (2024).
13. Z. Bai, X. Fan, X. Han, *et al.*, "Neuromorphic synaptic applications of oxygen-deficient BaSnO<sub>3</sub> thin films," *Appl. Phys. Lett.* **126**, 021905 (2025).
14. R. Li, Y. Dong, F. Qian, *et al.*, "CsPbBr<sub>3</sub>/graphene nanowall artificial optoelectronic synapses for controllable perceptual learning," *Photonix* **4**, 4 (2023).

15. H. Guo, J. Guo, Y. Wang, *et al.*, "An organic optoelectronic synapse with multilevel memory enabled by gate modulation," *ACS Appl. Mater. Inter.* **16**, 66948 (2024).
16. G. Agnus, W. Zhao, V. Derycke, *et al.*, "Two-terminal carbon nanotube programmable devices for adaptive architectures," *Adv. Mater.* **22**, 702 (2010).
17. Y. Li and G. Shen, "Advances in optoelectronic artificial synapses," *Cell Rep. Phys. Sci.* **3**, 101037 (2022).
18. Y. X. Hou, Y. Li, Z. C. Zhang, *et al.*, "Large-scale and flexible optical synapses for neuromorphic computing and integrated visible information sensing memory processing," *ACS Nano* **15**, 1497 (2021).
19. W. Huang, H. Zhang, J. Tang, *et al.*, "Self-powered optoelectronic synaptic devices for neuromorphic computing with the lowest energy consumption density," *ACS Photonics* **11**, 3095 (2024).
20. C. Kai, Y. Wang, X. Liu, *et al.*, "AlGaIn/GaN-based optoelectronic synaptic devices for neuromorphic computing," *Adv. Opt. Mater.* **11**, 2202105 (2023).
21. J. Feldmann, N. Youngblood, C. D. Wright, *et al.*, "All-optical spiking neuro-synaptic networks with self-learning capabilities," *Nature* **569**, 208 (2019).
22. F. Guo, M. Song, M. C. Wong, *et al.*, "Multifunctional optoelectronic synapse based on ferroelectric van der Waals heterostructure for emulating the entire human visual system," *Adv. Funct. Mater.* **32**, 2108014 (2021).
23. F. Tan, C. Chang, N. Zhang, *et al.*, "Physisorption-assisted optoelectronic synaptic transistors based on Ta<sub>2</sub>NiSe<sub>5</sub>/SnS<sub>2</sub> heterojunction from ultraviolet to near-infrared," *Light Sci. Appl.* **14**, 122 (2025).
24. J. Yu, X. Yang, G. Gao, *et al.*, "Bioinspired mechano-photonic artificial synapse based on graphene/MoS<sub>2</sub> heterostructure," *Sci. Adv.* **7**, eabd9117 (2021).
25. M. Farronato, P. Mannocci, M. Melegari, *et al.*, "Reservoir computing with charge-trap memory based on a MoS<sub>2</sub> channel for neuromorphic engineering," *Adv. Mater.* **35**, 2205381 (2022).
26. B. Lin, K. P. Ong, T. Yang, *et al.*, "Ultra-high electromechanical response from competing ferroic orders," *Nature* **633**, 798 (2024).
27. J. U. Woo, I. S. Kim, B. Kim, *et al.*, "Physical properties of crystalline NaNbO<sub>3</sub> thin film grown on Sr<sub>2</sub>Nb<sub>3</sub>O<sub>10</sub> nanosheets at low temperatures for piezoelectric energy harvesters," *Appl. Surf. Sci.* **593**, 153464 (2022).
28. M. H. Zhang, H. Ding, S. Egert, *et al.*, "Tailoring high-energy storage NaNbO<sub>3</sub>-based materials from antiferroelectric to relaxor states," *Nat. Commun.* **14**, 1525 (2023).
29. T. H. Lee, H. G. Hwang, J. U. Woo, *et al.*, "Synaptic plasticity and metaplasticity of biological synapse realized in a KNbO<sub>3</sub> memristor for application to artificial synapse," *ACS Appl. Mater. Inter.* **10**, 25673 (2018).
30. T. H. Lee, H. G. Hwang, S. Jang, *et al.*, "Low-temperature-grown KNbO<sub>3</sub> thin films and their application to piezoelectric nanogenerators and self-powered ReRAM device," *ACS Appl. Mater. Inter.* **9**, 43220 (2017).
31. B. Y. Kim, W. H. Lee, H. G. Hwang, *et al.*, "Resistive switching memory integrated with nanogenerator for self-powered bioimplantable devices," *Adv. Funct. Mater.* **26**, 5211 (2016).
32. B. Gaggio, A. Jan, M. Muller, *et al.*, "Sodium-controlled interfacial resistive switching in thin film niobium oxide for neuromorphic applications," *Chem. Mater.* **36**, 5764 (2024).
33. I. S. Kim, B. Kim, S. J. Chae, *et al.*, "Realization of self-rectifying and self-powered resistive random-access memory memristor using [001]-oriented NaNbO<sub>3</sub> film deposited on Sr<sub>2</sub>Nb<sub>3</sub>O<sub>10</sub> nanosheet at low temperatures," *Adv. Intell. Syst.* **6**, 2300634 (2023).
34. H. Dong, B. Luo, Z. Liu, *et al.*, "Electrical study of antiferroelectric NaNbO<sub>3</sub> thin films integrated directly on 4H-SiC," *J. Phys. Chem. Solids* **143**, 109477 (2020).
35. B. Luo, H. Dong, D. Wang, *et al.*, "Larger recoverable energy density with excellent thermal stability in Mn-modified NaNbO<sub>3</sub>-CaZrO<sub>3</sub> lead-free thin films," *J. Am. Ceram. Soc.* **101**, 3460 (2018).
36. Y. Zhang, Y. Niu, Y. Sun, *et al.*, "Effect of annealing temperature on energy storage performance of NaNbO<sub>3</sub>-based thin films under pure oxygen," *Appl. Phys. A-Mater.* **130**, 676 (2024).
37. W. Zeng, X. Niu, Y. Jiang, *et al.*, "An ultrahigh energy storage density in lead-free Na<sub>0.5</sub>Bi<sub>0.5</sub>TiO<sub>3</sub>-NaNbO<sub>3</sub> based ceramics via multiple optimization strategies," *Scr. Mater.* **245**, 116052 (2024).
38. H. Dong, B. Luo, and K. Jin, "Tunable dielectric and energy storage properties in nonstoichiometric NaNbO<sub>3</sub> thin films," *Ceram. Int.* **48**, 16215 (2022).
39. Z. Yang, H. Du, L. Jin, *et al.*, "A new family of sodium niobate-based dielectrics for electrical energy storage applications," *J. Eur. Ceram. Soc.* **39**, 2899 (2019).
40. K. R. Balasubramanian, K. C. Chang, F. A. Mohammad, *et al.*, "Growth and structural investigations of epitaxial hexagonal YMnO<sub>3</sub> thin films deposited on wurtzite GaN(001) substrates," *Thin Solid Films* **515**, 1807 (2006).
41. H. Zeng, L. Hao, W. Luo, *et al.*, "Trapping properties of LiNbO<sub>3</sub>/AlGaIn/GaN metal-ferroelectric-semiconductor heterostructure characterized by temperature dependent conductance measurements," *J. Appl. Phys.* **107**, 084508 (2010).
42. G. Leonetti, M. Fretto, F. C. Pirri, *et al.*, "Effect of electrode materials on resistive switching behaviour of NbO<sub>x</sub>-based memristive devices," *Sci. Rep.* **13**, 17003 (2023).
43. F. Opoku, K. K. Govender, C. G. C. E. Sittert, *et al.*, "Tuning the electronic structures, work functions, optical properties and stability of bifunctional hybrid graphene oxide/V-doped NaNbO<sub>3</sub> type-II heterostructures: A promising photocatalyst for H<sub>2</sub> production," *Carbon* **136**, 187 (2018).
44. B. Ofoonye, J. Lee, M. Yan, *et al.*, "Electrical and microstructural properties of thermally annealed Ni/Au and Ni/Pt/Au Schottky contacts on AlGaIn/GaN heterostructures," *Semicond. Sci. Technol.* **29**, 095005 (2014).
45. D. Gu, S. K. Dey, and P. Majhi, "Effective work function of Pt, Pd, and Re on atomic layer deposited HfO<sub>2</sub>," *Appl. Phys. Lett.* **89**, 082907 (2006).
46. F. C. Chiu, "A review on conduction mechanisms in dielectric films," *Adv. Mater. Sci. Eng.* **2014**, 578168 (2014).
47. K. F. Young and H. P. R. Frederikse, "Compilation of the static dielectric constant of inorganic solids," *J. Phys. Chem. Ref. Data* **2**, 313 (1973).
48. M. A. Lampert, "Simplified theory of space-charge-limited currents in an insulator with traps," *Phys. Rev.* **103**, 1648 (1956).
49. J. C. Phillips, "Stretched exponential relaxation in molecular and electronic glasses," *Rep. Prog. Phys.* **59**, 1133 (1996).
50. L. Zhou, J. Y. Mao, Y. Ren, *et al.*, "Biological spiking synapse constructed from solution processed bimetal core-shell nanoparticle based composites," *Small* **14**, 1800288 (2018).
51. B. Li, Y. Liu, C. Wan, *et al.*, "Mediating short-term plasticity in an artificial memristive synapse by the orientation of silica mesopores," *Adv. Mater.* **30**, 1706395 (2018).
52. Z. Li, G. Zou, Y. Xiao, *et al.*, "MoS<sub>2</sub>/ZnO-heterostructured optoelectronic synapse for multiwavelength optical information-based sensing, memory, and processing," *Nano Energy* **127**, 109733 (2024).
53. T. Zhang, C. Fan, L. Hu, *et al.*, "A reconfigurable all-optical-controlled synaptic device for neuromorphic computing applications," *ACS Nano* **18**, 16236 (2024).
54. X. Liu, D. Wang, W. Chen, *et al.*, "Optoelectronic synapses with chemical electric behaviors in gallium nitride semiconductors for biorealistic neuromorphic functionality," *Nat. Commun.* **15**, 7671 (2024).
55. M. Lee, W. Lee, S. Choi, *et al.*, "Brain-inspired photonic neuromorphic devices using photodynamic amorphous oxide semiconductors and their persistent photoconductivity," *Adv. Mater.* **29**, 1700951 (2017).
56. S. G. Hu, Y. Liu, T. P. Chen, *et al.*, "Emulating the Ebbinghaus forgetting curve of the human brain with a NiO-based memristor," *Appl. Phys. Lett.* **103**, 133701 (2013).
57. Z. Xiao and J. Huang, "Energy-efficient hybrid perovskite memristors and synaptic devices," *Adv. Electron. Mater.* **2**, 1600100 (2016).